

# DETECTING DARK MATTER-DARK ENERGY COUPLING WITH THE HALO MASS FUNCTION

P. M. SUTTER

Department of Physics, University of Illinois at Urbana-Champaign, Urbana, IL 61801-3080

AND

P. M. RICKER

Department of Astronomy, University of Illinois at Urbana-Champaign, Urbana, IL 61801  
 National Center for Supercomputing Applications, University of Illinois at Urbana-Champaign, Urbana, IL 61801

*Draft version November 6, 2018*

## ABSTRACT

We use high-resolution simulations of large-scale structure formation to analyze the effects of interacting dark matter and dark energy on the evolution of the halo mass function. Using a chi-square likelihood analysis, we find significant differences in the mass function between models of coupled dark matter-dark energy and standard concordance cosmology ( $\Lambda$ CDM) out to redshift  $z = 1.5$ . We also find a preliminary indication that the Dark Energy Survey should be able to distinguish these models from  $\Lambda$ CDM within its mass and redshift constraints. While we can distinguish the effects of these models from  $\Lambda$ CDM cosmologies with different fundamental parameters, DES will require independent measurements of  $\sigma_8$  to confirm these effects.

*Subject headings:* cosmology:theory, dark matter, dark energy, structure formation, methods: N-body simulations

## 1. INTRODUCTION

Multiple independent lines of evidence, including observations of the large-scale matter distribution (eg. Percival et al. 2001), cosmic microwave background fluctuations (eg. Hinshaw et al. 2008), and type Ia supernovae (Perlmutter et al. 1999; Riess et al. 1998), suggest that our universe is dominated by two components: dark matter, which is probably a form of non-baryonic matter, and dark energy, which is a name for the presently unknown cause of the observed acceleration of expansion. However, we still lack an understanding of any possible interactions between these two principal constituents (Bean et al. 2005). In a previous paper (Sutter & Ricker 2008; hereafter SR08), we examined the role that interacting dark matter and dark energy would play in the development of one-dimensional Zel'dovich pancakes, an important idealized case useful for understanding structure formation. Here we extend that preliminary work to a more realistic three-dimensional simulation of the growth of dark matter halos in an attempt to find ways to distinguish these models from standard cosmology.

In this paper, we study the effects of a Yukawa interaction between a single family of nonrelativistic dark matter (DM) particles and a scalar field that is responsible for the dark energy (DE). We follow closely the formalism developed by Farrar & Peebles (2004). Such an interaction is initially attractive because it is motivated by particle physics (Amendola 2000) and might provide a way to explain the apparent emptiness of the voids, as demonstrated numerically by Nusser, Gubser, & Peebles (2005).

There has been considerable interest recently in studying the effects of these interactions on structure, both using an analytic approach (Mainini & Bonometto 2006)

and using direct simulations (eg. Macciò et al. 2004; Manera & Mota 2006; and others). However, the current numerical studies suffer from poor resolution, and these results cannot reliably be compared to simulations of standard cosmological structure formation. In this paper, we use high spatial resolution and careful analysis to accurately capture many dark matter halos for use in comparison.

The following is a brief summary of the equations we solve and our numerical techniques. In Section 2 we discuss modifications to the halo mass function. We use these mass functions to distinguish interacting DM-DE from standard concordance cosmology using a  $\chi^2$  likelihood test. Additionally, we discuss the feasibility of using the Dark Energy Survey (Annis et al. 2005) to detect this coupling within its mass and redshift constraints. Finally, we determine the extent to which two specific models of interacting DM-DE can be differentiated from each other.

### 1.1. Analytical Methods

Compared to simulations of the full non-linear theory, we found in SR08 that the perturbation theory presented by Farrar and Peebles is very accurate in determining the evolution of structure, and hence we will maintain the perturbative approach and assume fluctuations in the scalar field are small. Under perturbation theory, the homogeneous part of the dark energy scalar field,  $\phi_b$ , evolves as

$$\ddot{\phi}_b + 3\frac{\dot{a}}{a}\dot{\phi}_b + \frac{dV}{d\phi_b} + 3\frac{\Omega_{m0}H_0^2}{8\pi G}\frac{1}{\phi_b}a^{-3} = 0, \quad (1)$$

where  $\Omega_{m0}$  is the dark matter particle fraction of the critical density and  $H_0$  is the Hubble constant. A subscript of 0 denotes the present-day value. The dark matter particle equation of motion is

$$\dot{\mathbf{v}} + \left(2\frac{\dot{a}}{a} + \frac{\dot{\phi}_b}{\phi_b}\right)\mathbf{v} = -\left(1 + \frac{1}{4\pi G}\frac{1}{\phi_b^2}\right)\nabla\Phi. \quad (2)$$

Label	$\alpha$	$K(G^{1+\alpha/2}/H_0^2)$	$\phi_{\text{init}}(G^{1/2})$	$\phi_0(G^{1/2})$
A	-2	0.03	1.89	1.72
B	6	2.0	1.80	1.68

TABLE 1  
SIMULATION POTENTIAL PARAMETER VALUE CHOICES.

Here  $\Phi$  is the normal comoving gravitational potential,  $a$  is the scale factor,  $\mathbf{v}$  is the comoving particle peculiar velocity, and  $\mathbf{x}$  is the comoving position. Throughout, dots refer to derivatives with respect to proper time  $t$ . Perturbations in the scalar field give rise to the fifth force on the right-hand side in the equation above.

The comoving potential satisfies the Poisson equation:

$$\nabla^2 \Phi = \frac{4\pi G}{a^3} (\rho - \bar{\rho}), \quad (3)$$

with  $\rho$  as the comoving DM particle density. Here and throughout, an overline indicates a spatial average.

At the present epoch, the field behaves as a cosmological constant, so the potential term in Eq.(1) dominates and has a value

$$V(\phi_{b,0}) = \Omega_{\Lambda 0} \rho_{\text{crit}}. \quad (4)$$

At early times, the coupling to matter dominates the scalar field equation of motion, and Eq. (1) reduces to

$$\frac{d\phi_b}{dt} = -\frac{H_0^2}{G} \frac{3\Omega_{m0}}{8\pi\phi_0} \frac{1}{a^3} t, \quad (5)$$

which we use to set the initial condition for  $\dot{\phi}_b$ .

The DM particle also has a field-dependent mass

$$m_{DM} = m_{DM,0} \frac{\phi_b}{\phi_{b,0}}. \quad (6)$$

The Friedmann equation, neglecting radiation, curvature, and baryonic terms, becomes

$$\left(\frac{\dot{a}}{a}\right)^2 = H_0^2 \Omega_{m0} \frac{\phi_b}{\phi_{b,0}} a^{-3} + \frac{8\pi G}{3} \left[ \frac{1}{2} \left(\frac{d\phi_b}{dt}\right)^2 + V(\phi_b) \right]. \quad (7)$$

To simulate a comparative  $\Lambda$ CDM cosmology, we fixed  $\phi_b$  to the value in Eq.(4) and prevented any interactions between the field and particles.

### 1.2. Numerical Methods

We study a general power-law potential:

$$V(\phi) = K/\phi^\alpha, \quad (8)$$

where we are free to choose the constants  $K$  and  $\alpha$ . Based on the comments made by Farrar and Peebles and our analysis in SR08, we chose two combinations of parameters. These were selected for behaviors that were significantly different from standard cosmologies, but not drastic enough to rule them out with current observational constraints. Table 1 lists the parameter values, the guessed initial field value at our simulation initial redshift, and the field value today as calculated from Eq. (1).

For our simulations we chose FLASH v2.5, an adaptive-mesh refinement (AMR) code for astrophysics and cosmology (Fryxell et al. 2000). FLASH solves the N-body potential problem with a particle-mesh multigrid FFT method (Ricker 2008). FLASH uses cloud-in-cell mapping for interpolating between the mesh and particles (Hockney & Eastwood 1988) and a second-order

leapfrog integration scheme for variable-timestep particle advancement. We modified the standard FLASH code by adding the additional drag and force terms from Eq. (2). At each timestep, the particle mass is updated according to Eq. (6). We calculate the scale factor and scalar field value in-code by numerically solving Eqs. (7) and (1), respectively. For a more detailed explanation of solving the scalar field equation, see SR08.

For all calculations, we used concordance parameter values of  $\Omega_{m0} = 0.26$ ,  $\Omega_{\Lambda 0} = 0.74$ , and  $H_0 = 100h = 71 \text{ km s}^{-1} \text{ Mpc}^{-1}$ . All runs took place in a three-dimensional box measuring  $128 h^{-1} \text{ Mpc}$  per side with  $256^3$  particles. For each model, including a  $\Lambda$ CDM reference, we performed 10 simulations with 512 zones per side and an additional 4 simulations with 1024 zones per side to study lower mass ranges. There was no refinement of grid spacing. All simulations used the same initial conditions: unperturbed particle positions were situated on a grid, and the initial velocities and positions were perturbed using Gaussian fluctuations normalized to  $\sigma_8 = 0.751$ . We assumed P(k) from a  $\Lambda$ CDM cosmology. We used the GRAFIC2 code (Bertschinger 2001) to generate these initial conditions. All computations started at a redshift of  $z = 56.8$ .

We used a friends-of-friends (FOF) routine to find halos. This algorithm builds lists of all particles that are within a certain maximum distance of their neighbors. For all results, we chose a linking distance of  $1/5$  of the unperturbed particle spacing, which is  $500 h^{-1} \text{ kpc}$ . At every analysis redshift, we calculated the minimum resolvable halo particle count according to the prescription in Lukić et al. (2007):

$$n_{h,\text{min}} = \frac{\Delta(1.62n_p/n_g)^3}{\Omega_{m0}(1+z)^3} [\Omega_{m0}(1+z)^3 + \Omega_{\Lambda 0}], \quad (9)$$

where  $n_g$  and  $n_p$  are the number of zones and particles per side, respectively. We chose an overdensity factor of  $\Delta = 200$ . To examine the halo mass function, we corrected the halo FOF particle counts by the factor given in Warren et al. (2006):

$$n_h^{\text{corr}} = n_h(1 - n_h^{-0.6}). \quad (10)$$

### 2. THE HALO MASS FUNCTION

Figure 1 shows the relative mass function from redshift  $z = 0$  to  $z = 1.5$  for the two models listed above. Both of these are compared to the  $\Lambda$ CDM simulation mass function. We will use the frequency density definition of the mass function,

$$F(M, z) \equiv \log \frac{dn}{d \log M}, \quad (11)$$

so that for model  $i$  we may define the relative mass function as

$$RF(M, z)_i \equiv \log \frac{dn}{d \log M} \Big|_i - \log \frac{dn}{d \log M} \Big|_{\Lambda\text{CDM}}. \quad (12)$$

We analyzed relative mass functions to reduce any systematic errors in the simulations, including those due to small box effects, such as missing tidal forces. We binned our distributions into 10 fixed logarithmic intervals from  $10^{11.5}$  to  $10^{15} h^{-1} M_\odot$ . We only display values in bins for which we have complete data (i.e. the bin does not

contain the minimum resolvable mass). The uncertainties shown are obtained by summing in quadrature the individual statistical counting errors in the interacting and  $\Lambda$ CDM cases. We see that at the present epoch, both models produce a greater number of the most massive halos while underproducing low-mass objects. At higher redshifts, both models produce greater numbers of all objects. Since the relative mass function does not remain constant with redshift, it is distinguishable from a concordance cosmology with different fundamental parameters.

To determine the significance of these mass function differences, we performed a  $\chi^2$  likelihood test at each redshift. For two independent frequency distributions  $R$  and  $S$ ,

$$\chi^2 = \sum_i \frac{(S_i - R_i)^2}{S_i + R_i}, \quad (13)$$

where the sum takes place over all bins and the number of degrees of freedom is the total number of non-zero bins. Figure 2 shows the probability at each redshift that the frequency distributions from the interacting cases are consistent with the  $\Lambda$ CDM case. We see that for almost all redshifts, the probability is exceedingly small, indicating that these coupled DM-DE models are well distinguished from  $\Lambda$ CDM cosmology with this sample of objects. As a function of redshift, the probability for both models generally decreases. For model *A* at  $z = 0.5$ , however, these distributions are not well separated, since this is the redshift at which the mass functions come closest. Model *B* remains indistinct from  $\Lambda$ CDM until  $z = 0.5$ , at which point the separation becomes progressively more evident. The probabilities for both models drop below  $10^{-10}$  at redshifts  $z = 0.75$  and  $z = 1.5$  and are not shown at higher redshifts.

To determine the feasibility of using a survey like DES to detect these models, we need to know the expected frequency distribution of observed objects in the survey, since the fundamental uncertainty arises from counting errors. While the exact selection function for DES has not yet been determined, the survey is expected to capture  $\sim 10,000$  objects of mass  $> 10^{13.5} h^{-1} M_\odot$  out to redshift  $z \sim 1.5$  (The Dark Energy Survey, White Paper submitted to the Dark Energy Task Force in 2005). Our combined simulations produced roughly this many objects in this mass and redshift range. Figure 2 shows the  $\chi^2$  probability when only considering mass bins above  $10^{13.5} h^{-1} M_\odot$ . With this cut the probability suffers; however, we maintain the general trend of increased disparity with higher redshift. For both models, the greatest deviations occur at  $z = 0.75$  and  $z = 1.5$ . The probabilities at these redshifts are below the common significance threshold and indicate that DES is capable of detecting these models. At lower redshifts, there is not a significant difference in the number of high-mass objects. Between these redshifts, the uncertainties in the largest mass bins are too large to make a confident distinction between the distributions.

It is possible to observe similar deviations in the mass function by changing the fundamental parameters of a  $\Lambda$ CDM cosmology, such as  $\Omega_{m0}$  and  $\sigma_8$ . We could not find any combination of fundamental parameters that reproduced these relative mass functions for all mass bins and redshifts. However, when examining masses within

the DES limit, there are degeneracies. For example, Figure 1 shows the relative mass function, obtained using the Warren et al. (2006) analytic mass function, of two  $\Lambda$ CDM cosmologies with different values of  $\sigma_8$ . In this case, we compared a  $\sigma_8$  of 0.751, which we used in our simulations, to a cosmology with  $\sigma_8 = 0.775$ . We chose this value to mimic the entire relative mass function at high redshift, but it does not capture the counts of lower-mass objects at low redshift. However, above  $10^{13.5} h^{-1} M_\odot$ , the uncertainties are large enough to permit this modified  $\sigma_8$  to adequately fit the data. Thus, DES alone may not be able to distinguish between a universe with interacting DM-DE and a universe with higher  $\sigma_8$ .

While these two models are easily distinguishable from  $\Lambda$ CDM cosmology, they are more difficult to differentiate from each other. Figure 3 shows the  $\chi^2$  probability when comparing these two models, both for all masses and DES-accessible masses. When including all masses, the probabilities are significant at redshifts  $z = 0.0, 1.0$ , and  $1.5$ . However, when examining only masses available to DES, the probabilities maintain a roughly constant performance and never reach a significant level.

### 3. CONCLUSIONS

We have found that coupling dark matter to a dark energy scalar field produces significantly different mass functions at redshifts as high as  $z = 1.5$  relative to a  $\Lambda$ CDM cosmology with the same set of fundamental parameters. This difference in the mass function follows from our analysis in SR08: an additional fifth force and a reduced particle Hubble drag lead to more structures than in  $\Lambda$ CDM cosmologies at early times, and at late times will cause an overabundance of high-mass objects and a subsequent reduction in low-mass cluster counts. By examining the mass function, we have developed a simple way of distinguishing these models. This analysis allows us to discover ways of further constraining different parameters of DM-DE coupling.

We have found that the statistical uncertainties in the mass function do not prevent the Dark Energy Survey from detecting this form of coupled dark matter and dark energy. Once the selection function for DES is known, a detailed study will need to take place. However, we have found that DES alone will have difficulty differentiating among different sets of parameters that control the coupling.

At high masses the statistical uncertainties may prevent DES from distinguishing between coupled DM-DE and  $\Lambda$ CDM cosmologies with different values of  $\sigma_8$ . We can overcome this degeneracy in several ways. First, missions such as Planck (Tauber 2000) can independently constrain  $\sigma_8$  and  $\Omega_{m0}$ . If DES prefers a higher value of  $\sigma_8$  through the mass function, this may be explained by interacting dark matter and dark energy. Secondly, more detailed measurements of the halo mass function from projects such as LSST (Sweeney 2006) will tightly constrain the mass function at multiple redshifts. Also, DES itself may detect more clusters than our estimated 10,000. A universe with coupled DM-DE will then produce an apparently redshift-dependent  $\sigma_8$ .

It will also be necessary to compare these mass functions to those produced by modified General Relativity

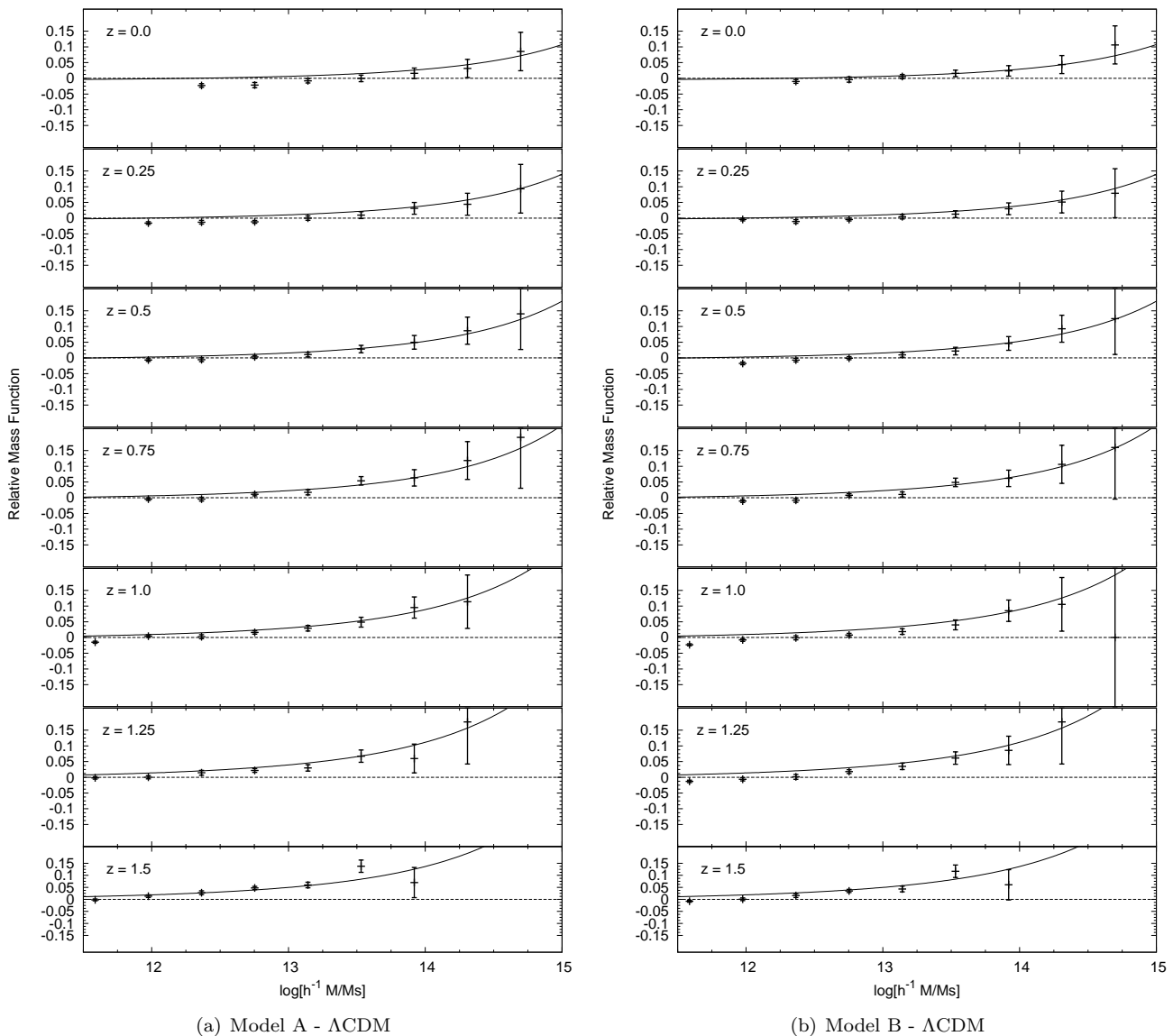


FIG. 1.— Relative mass functions for the power-law potentials.. The plots are labeled as in Table 1. Error bars are at one standard deviation and come from statistical counting uncertainties. The solid curve is the relative mass function of two  $\Lambda$ CDM cosmologies with  $\sigma_8 = 0.775$  and  $\sigma_8 = 0.751$ .

(such as those found in Stabenau & Jain (2006)), as both theories modify the Poisson equation, and hence can in principle have similar effects.

#### ACKNOWLEDGMENTS

The authors acknowledge support under a Presidential Early Career Award from the U.S. Department of Energy, Lawrence Livermore National Laboratory (con-

tract B532720). Additional support was provided by a DOE Computational Science Graduate Fellowship (DE-FG02-97ER25308) and the National Center for Supercomputing Applications. The software used in this work was in part developed by the DOE-supported ASC / Alliance Center for Astrophysical Thermonuclear Flashes at the University of Chicago.

#### REFERENCES

- Amendola, L. 2000, *Phys. Rev. D*, 62, 043511  
 Annis, J. et al. 2005  
 Bean, R., Carroll, S., & Trodden, M. 2005, *astro-ph/0510059*  
 Bertschinger, E. 2001, *ApJS*, 137, 1  
 Farrar, G. R. & Peebles, P. 2004, *ApJ*, 604, 1  
 Fryxell, B. et al. 2000, *ApJS*, 131, 273  
 Hinshaw, G. et al. 2008, *ArXiv e-prints*, 803  
 Hockney, R. W. & Eastwood, J. W. 1988, *Computer Simulation using Particles* (Bristol: Hilger)  
 Lukić, Z., Heitmann, K., Habib, S., Bashinsky, S., & Ricker, P. M. 2007, *ApJ*, 671, 1160  
 Macciò, A. V., Quercellini, C., Mainini, R., Amendola, L., & Bonometto, S. A. 2004, *Phys. Rev. D*, 69, 123516  
 Mainini, R. & Bonometto, S. 2006, *Phys. Rev. D*, 74, 043504  
 Manera, M. & Mota, D. F. 2006, *MNRAS*, 371, 1373  
 Nusser, A., Gubser, S., & Peebles, P. 2005, *Phys. Rev. D*, 71, 083505  
 Olivares, G., Atrio-Barandela, F., & Pavón, D. 2006, *Phys. Rev. D*, 74, 043521  
 Percival, W. J. et al. 2001, *MNRAS*, 327, 1297  
 Perlmutter, S. et al. 1999, *ApJ*, 517, 565  
 Ricker, P. M. 2008, *ApJS*, in press  
 Riess, A. G. et al. 1998, *AJ*, 116, 1009  
 Stabenau, H. & Jain, B. 2006, *Phys. Rev. D*, 74, 084007

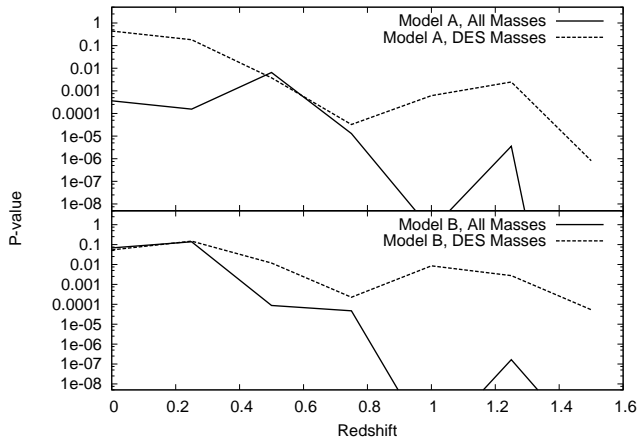


FIG. 2.— Probability for the chi-square statistic as a function of redshift for model A (top) and model B (bottom) compared to  $\Lambda$ CDM. The solid lines are from including all resolvable masses, and the dashed lines are from only considering objects with  $M_{FOF} > 10^{13.5} h^{-1} M_{\odot}$ .

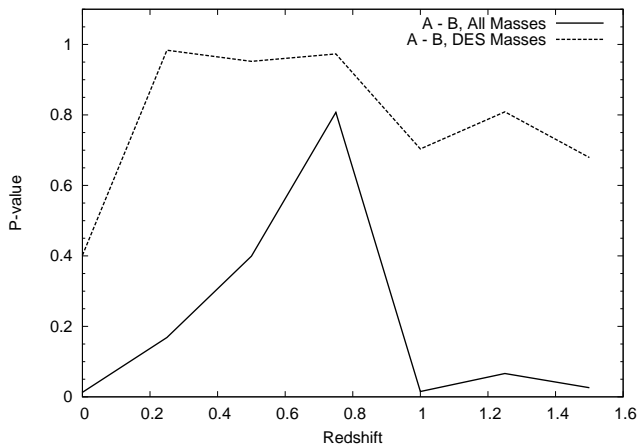


FIG. 3.— Probability for the chi-square statistic as a function of redshift for model A compared to model B. The solid line is from including all resolvable masses, and the dashed line is from only considering objects with  $M_{FOF} > 10^{13.5} h^{-1} M_{\odot}$ .

- Sweeney, D. W. 2006, in *Ground-based and Airborne Telescopes*. Edited by Stepp, Larry M.. Proceedings of the SPIE, Volume 6267, pp. 626706 (2006)., Vol. 6267
- Tauber, J. A. 2000, in *ESA Special Publication*, Vol. 455, ISO Beyond Point Sources: Studies of Extended Infrared Emission, ed. R. J. Laureijs, K. Leech, & M. F. Kessler, 185–+
- The Dark Energy Survey, White Paper submitted to the Dark Energy Task Force. 2005
- Warren, M., Abazajian, K., Holz, D., & Teodoro, L. 2006, *ApJ.*, 646, 881